

Real-time Coordination of Cascaded Hydroelectric Generation under Decision-Dependent Uncertainties

Eliza Cohn, *Student Member, IEEE*, Ning Qi, *Member, IEEE*, Upmanu Lall, and Bolun Xu, *Member, IEEE*

Abstract—This paper proposes a real-time control policy for cascaded hydropower systems that incorporates decision-dependent uncertainty (DDU) to capture the coupling of streamflow uncertainties across the network. The framework jointly models exogenous forecast errors and endogenous uncertainty propagation, explicitly characterizing the dependence between upstream releases and downstream inflow variability through a heteroskedastic variance model conditioned on past errors, variance, and control actions. We formulate a joint chance-constrained optimization problem to ensure reliable system operation under uncertainty, and develop a tractable supporting hyperplane algorithm that enables explicit and adaptive risk allocation under DDU. We establish convergence of the proposed method and show that it recovers the Bonferroni approximation under steady-state conditions. A randomized case study based on Columbia River data demonstrates that the proposed framework improves both energy generation and reservoir reliability by accounting for DDU. Sensitivity analyses on drought severity and model parameters further highlight the value of adaptive risk allocation for resilient hydropower operations.

Index Terms—Cascaded hydropower, non-anticipatory control, decision-dependent uncertainty, joint chance-constrained optimization, short-term dispatch.

I. INTRODUCTION

Ensuring reliable power supply from cascaded hydropower systems is challenging due to spatiotemporal uncertainty in networked streamflows [1]. The operation of such systems must account not only for exogenous uncertainty—such as seasonality and weather variability—but also for endogenous effects arising from upstream release decisions that influence downstream inflows and subsequent control actions. This interplay induces strong spatial and temporal coupling across the network, resulting in a high-dimensional stochastic control problem. Such a structure motivates a framework that explicitly captures endogenous (decision-dependent) uncertainty [2].

Previous work mostly approximates the coupling between reservoirs using deterministic mass-balance equations, in which upstream releases are routed downstream via fixed travel-time delays. Such models have been widely adopted in deterministic optimization that assumes static flow [3]–[5]; two-stage stochastic optimization, where medium-term planning determines target reservoir levels based on seasonal forecasts, followed by short-term hourly scheduling [6], [7];

and multi-stage stochastic dual dynamic programming (SDDP) frameworks, in which inflow uncertainty is typically modeled as an exogenous stochastic process [8], [9]. While this captures the physical connectivity of the cascade, it assumes that upstream outflows translate directly to downstream inflows without modifying the uncertainty structure. As a result, these models do not capture how upstream operational decisions influence the variability or distribution of downstream inflows. These models are also primarily designed for multi-stage planning and may be less suited to real-time adaptation when uncertainty evolves in response to upstream decisions.

From a hydrologic perspective, flow propagation in river networks is a stochastic transport process rather than a simple deterministic delay. Classical models, such as unit hydrograph theory and linear system representations, describe downstream flow as a distributed and attenuated response to upstream inputs, shaped by travel time, dispersion, and local inflows [10], [11]. River routing further introduces state-dependent and heteroskedastic behavior, where channel conditions and release decisions affect both the mean and variability of streamflow [12], [13]. As a result, upstream releases can amplify or redistribute uncertainty across the cascade, inducing spatially correlated and decision-dependent uncertainty. Modeling inflows as exogenous or independent therefore fails to capture these dynamics, motivating a framework that explicitly accounts for endogenous coupling between control actions and uncertainty evolution. Although decision-dependent uncertainty (DDU) has been explored in power system planning [14], [15] and operations [16], [17], its application to modeling uncertainty propagation and coupling in cascaded hydropower systems remains largely unexplored.

This paper proposes a real-time control policy for cascaded hydropower systems under DDU, explicitly capturing the coupling of streamflow uncertainties across the cascade. The proposed framework strengthens the water–energy nexus by improving the reliability of energy supply and reservoir water management. Our main contributions are as follows:

- 1) *Modeling*: We propose a cascaded hydropower streamflow model that jointly captures exogenous forecast errors and endogenous uncertainty propagation, explicitly characterizing the dependence between upstream releases and downstream inflow variability through a heteroskedastic variance model conditioned on past errors, past variance, and control actions.
- 2) *Methodology*: We formulate a joint chance-constrained optimization problem to ensure reliable system operation under DDU, and develop a tractable supporting hyperplane algorithm that enables explicit and adaptive

This paper was submitted for review on Feb X, 2026. This work was supported by the National Science Foundation Graduate Research Fellowship under Grant No. DGE-2036197.

Eliza Cohn, Ning Qi, and Bolun Xu are with the Department of Earth and Environmental Engineering, Columbia University, New York, NY 10027 USA (e-mail: ec376,nq2176,bx2177@columbia.edu). Upmanu Lall is with the School of Complex Adaptive Systems, Arizona State University, Tempe, AZ 85287 USA (e-mail: ulall@asu.edu).

risk allocation under DDU. We establish convergence of the proposed method and show that it recovers the Bonferroni approximation under steady-state conditions.

- 3) *Numerical study*: We introduce an integrated violation index to quantify the effectiveness and reliability of the proposed control policy. A randomized case study based on Columbia River data demonstrates that explicit consideration of DDU improves both energy generation and reservoir storage reliability. Sensitivity analyses on drought severity and DDU model parameters further highlight the value of adaptive risk allocation for resilient cascaded hydropower operation.

The remaining section of the paper are organized as follows. Section II presents the problem formulation and defines the uncertainty characteristics. Section III presents the supporting hyperplane solution algorithm and its benchmark, the Bonferroni approximation. Section IV tests the algorithm in a numerical case study that simulates a stochastic drought framework. Section V concludes the paper.

II. PROBLEM FORMULATION AND PRELIMINARIES

A. Formulation

We consider a networked system of cascaded hydropower reservoirs consisting of n units $\mathcal{I} = \{1, 2, \dots, n\}$ to be scheduled over the time horizon $\mathcal{T} = \{1, 2, \dots, T\}$. Each unit is connected in series along the same river, and the matrix of streamflow observations into each unit is denoted by $Q \in \mathbb{R}^{T \times n}$. The streamflow inputs into the hydropower reservoirs \hat{q}_t are modeled as a combination of the forecasted inflows μ_t predicted at the planning stage and the forecast deviations ξ_t revealed during real-time operations. We assume that ξ_t follows a distribution \mathbb{P} centered around 0, following [18].

Fig. 1 gives a stylized illustration of why hydropower units operating along the same river give rise to inflow forecast errors that are spatially correlated. Because we explicitly model this process uncertainty in forecasting inflow, it is necessary to incorporate bilateral joint chance constraints that calculate the probability of maintaining reservoir volumes between both the upper and lower bounds for all units while preserving spatial correlation under the forecast uncertainty. This form of the joint chance-constraint was proposed by [19] and has become the standard for modeling multi-use reservoirs that incorporate both hydrologic and energy dispatch needs [20]. This energy dispatch problem gives rise to the following stochastic program:

$$\max_{p, u, s, v} \sum_{i \in \mathcal{I}} \sum_{t \in \mathcal{T}} p_{i,t} \quad (1a)$$

$$\text{s.t. } v_{i,t} = v_{i,t-1} + \Delta_t (\hat{q}_{i,t} - u_{i,t}) \quad (1b)$$

$$p_{i,t} = c \eta g \rho \phi(v_{i,t}) u_{i,t} \quad (1c)$$

$$\underline{R} \leq u_{i,t} - u_{i,t-1} \leq \bar{R} \quad (1d)$$

$$\underline{U} \leq u_{i,t} \leq \bar{U} \quad (1e)$$

$$0 \leq p_{i,t} \leq \bar{P} \quad (1f)$$

$$\mathbb{P}[\underline{V}_i \leq v_{i,t} \leq \bar{V}_i] \geq 1 - \varepsilon \quad (1g)$$

TABLE I
NOMENCLATURE

Symbol	Description
Indices	
t	Index for time periods
i	Index for hydro unit
j	Index for upstream unit
n	Number of hydro units
Functions	
$\phi_i(\cdot)$	Hydraulic head function
$\mathbb{P}(\cdot)$	Probability measure over inflow uncertainty
Sets	
\mathcal{I}	Set of hydro units
\mathcal{T}	Set of time periods
Parameters	
ε	Risk tolerance
c	Conversion factor from J to MW (3.6×10^{-9})
Δ_t	Time step duration
g	Gravitational acceleration ($9.8m/s^2$)
η_i	Turbine efficiency
ρ	Density of water ($1000kg/m^3$)
Bounds / Limits	
\bar{P}	Transmission capacity (MW)
\bar{R}, \underline{R}	Ramp rates (m^3/s^2)
$\bar{V}_i, \underline{V}_i$	Volume bounds (m^3)
\bar{U}, \underline{U}	Turbine release bounds (m^3/s)
Model Parameters	
μ_t	Forecasted inflow (m^3/s)
ξ_t	Forecast uncertainty
Σ_t	System covariance matrix
α_0	Streamflow regression constant
α_n	Streamflow regression AR coefficient
β_m	Streamflow regression upstream release coefficient
ω	GARCH model constant
ξ	GARCH model previous error term coefficient
ζ	GARCH model previous std. coefficient
γ	GARCH model upstream release coefficient
Decision Variables	
$p_{i,t}$	Energy output (MWh)
$v_{i,t}$	Reservoir volume (m^3)
$u_{i,t}$	Reservoir generation outflow rate (m^3/s)
$\hat{q}_{i,t}$	Streamflow random variable (m^3/s)

The objective function (1a) reflects the operator's goal of maximizing power generation since hydropower has no marginal costs. Decision variable $p_t \in \mathbb{R}^n$ (MWh) denotes the dispatched energy for all hydropower units; $u_t \in \mathbb{R}^n$ (m^3) denotes the water release intended for generation; $s_t \in \mathbb{R}^n$ (m^3) denotes the remaining water release that becomes spill outflow; $v_t \in \mathbb{R}^n$ (m^3) denotes the reservoir volume at end of each time period. All decisions are made at the hourly time step. The constraint (1b) tracks the volume state in the reservoirs based on the stochastic inflow \hat{q}_t (m^3), previous volume v_{t-1} (m^3), and release decisions. The inflow forecast $\hat{q}_t \in \mathbb{R}^N$ is a linear combination of the deterministic mean forecast and the forecast uncertainty, and is characterized in

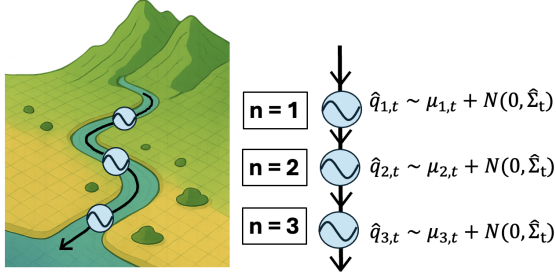


Fig. 1. Cascaded hydropower network with correlated inflows

II-B. The hydroelectric power production from water release is defined by (1c). A conversion from joule to MWh by parameter c ($1\text{MWh}=3.6e^9\text{Joule}$) ensures unit consistency on both sides of the constraint. (1d) models the water flow ramp rates \underline{R} and \overline{R} , (1e) models the upper and lower water release bounds \underline{U} and \overline{U} , and (1f) limits the total unit generation with the transmission capacity \overline{P} . The joint-chance constraint ensures volume bounds are satisfied with respect to inflow uncertainty is given in (1g), where ε represents the risk tolerance set by the operator. Applying chance constraints to the reservoir volume bounds is a critical step in encoding hydrologic uncertainty into a power system planning model.

Note that (1c) models the nonlinear hydraulic head function as a concave function between volume and height [21]. This exact form of the mapping from volume to head is typically fit from real-world data, and depends on the shape of the reservoir. This modeling framework follows the classical formulation of nonlinear cascaded hydropower optimization programs [3], [22]–[24]. A piece-wise linear approximation is applied to the nonlinear power production function in (1c) to both convexify the constraint and increase tractability. The linear approximation uses a set of 1-D functions to partition the hydraulic head into N sub-intervals. The algorithm is given in Appendix A. The linear approximation indexes the reference hydraulic head with the previous volume state decomposes the multi-period framework into a non-anticipatory framework that is solved sequentially for each time step, taking advantage of the nature of the two-stage scheduling process, since real-time decisions are finalized once the inflow forecast uncertainty is observed.

B. Inflow and Uncertainty Characterization

Real-time dispatch of hydroelectric operations relies on inflow forecasts that are inherently uncertain. We model the inflow random variable $\hat{q}_t \in \mathbb{R}^n$ as a multivariate Gaussian distribution whose mean equals the deterministic forecast and variance representing forecast uncertainty, which may vary over time [25]. Alternate distributions, such as the log-normal, can also be assumed in this framework. In that case, chance constraints would be evaluated using Monte Carlo sampling or moment-based bounds derived from the mean and covariance. The Gaussian assumption preserves analytical tractability of the resulting chance-constrained formulation. For each time step, we define the inflow distribution as

$$\hat{q}_t = \mu_t + \xi_t, \quad \xi_t \sim \mathcal{N}(0, \hat{\Sigma}_t) \quad (2)$$

where \hat{q}_t is the vector of random inflow realizations, μ_t denotes the deterministic inflow forecasts, and ξ_t represents the stochastic forecast error with spatial covariance Σ_t . The forecast for each unit is obtained via a linear regression model of the form

$$\mu_{i,t} = \alpha_0 + \sum_{n=1}^p \alpha_n q_{i,t-n} + \sum_{m=1}^q \beta_m u_{j,t-m} \quad (3)$$

where $q_{i,t-n}$ are previous observed inflow terms and $(u_{j,t-m} + s_{j,t-m})$ are previous water releases from the upstream unit. By including the local flow and system dynamics in the inflow forecast, we can capture both the effects of the surrounding ecosystem and the release decisions made by upstream units.

Let $\hat{q}_{i,t}$ denote the inflow forecast obtained from the regression model in (3), and let $q_{i,t}$ denote the observed inflow realization. The forecast residual is defined as

$$e_{i,t} = q_{i,t} - \hat{q}_{i,t}, \quad (4)$$

where we collect these into the residual vector $e_t = (e_{1,t}, \dots, e_{n,t})^T$.

Reservoir operators typically estimate deviations from inflow forecasts within a decision-independent framework, using historical data to calculate static uncertainty sets. However, this can lead to aggressive control policies, leaving little buffer room for handling extreme events. Decision-dependent uncertainty representations incorporate upstream release decisions into the estimation framework, quantifying how upstream units' release strategies affect the normal distribution's covariance matrix. We show that this enhanced modeling sensitivity can lead to more conservative variance estimates.

1) *Decision-Independent Uncertainty:* Under DIU, the covariance matrix is static and estimated offline from the residuals of historical streamflow forecasts. Let $e_t = (e_{1,t}, \dots, e_{n,t})^T$ denote the vector of forecast residuals. We then estimate the DIU forecast-error covariance matrix as

$$\hat{\Sigma}^{DIU} = \frac{1}{T-1} \sum_{t=1}^T (e_t - \bar{e})(e_t - \bar{e})^T \quad (5a)$$

$$\hat{\sigma}^{DIU} = \sqrt{\text{diag}(\hat{\Sigma}^{DIU})} \quad (5b)$$

The per-unit variance terms in (5b) are constant under the assumption of DIU. Because the covariance matrix is fixed over time, it is independent of operational decisions. Estimating the spatial variance from regression residuals captures the cross-unit forecast uncertainty not explained by the deterministic inflow model [26].

2) *Decision-Dependent Uncertainty:* Fig. 2 demonstrates the importance of incorporating decision-dependent uncertainty when modeling the heteroskedasticity of the inflow forecast error magnitude. Conditioning the forecast error on the upstream hydroelectric release shows that the magnitude of

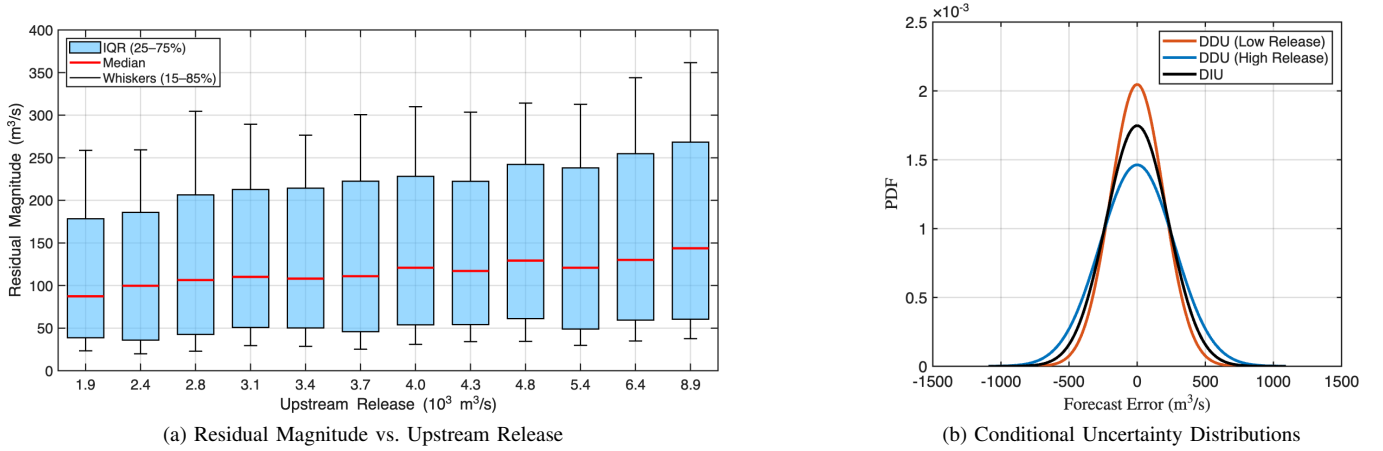


Fig. 2. Empirical characterization of DDU. (a) Residual magnitude increases with upstream release, demonstrating heteroskedastic forecast error. (b) Corresponding conditional normal distributions showing how DDU produces state-dependent variance to DIU.

forecast residuals grows as upstream releases increase. This effect is highlighted by plotting the conditional normal distributions of the forecast errors. Compared to DIU, which assumes a fixed variance regardless of decisions, DDU captures how the variability of outcomes changes with operational choices, providing a more accurate representation of risk that depends on prior releases. Under DIU, the assumed constant covariance matrix can lead to poorly calibrated reliability guarantees. Fig. 3 summarizes the learning algorithm that synthesizes offline parameter estimation with real-time state updates create the dynamic DDU covariance matrix given below:

$$\hat{\Sigma}_t^{DDU} = \begin{pmatrix} (\hat{\sigma}_{1,t}^{DDU})^2 & \dots & \hat{\rho}_{1n} \hat{\sigma}_{1,t}^{DDU} \hat{\sigma}_{n,t}^{DDU} \\ \vdots & \ddots & \vdots \\ \hat{\rho}_{n1} \hat{\sigma}_{n,t}^{DDU} \hat{\sigma}_{1,t}^{DDU} & \dots & (\hat{\sigma}_{n,t}^{DDU})^2 \end{pmatrix} \quad (6a)$$

$$\hat{\sigma}_{i,t}^{DDU} = \sqrt{\omega + \xi e_{i,t-1}^2 + \zeta \sigma_{i,t-1}^2 + \gamma u_{j,t-1}} \quad (6b)$$

Let $\rho_{i,j}$ refer to the correlation coefficient between the forecast residuals of units i and j . To model the time-varying volatility structure and capture the spatial correlation of inflows, we employ the generalized autoregressive conditional heteroskedasticity (GARCH) model proposed by Bollerslev in [27] to estimate the heteroskedastic variance as a linear combination of past squared residuals and past squared variance. We extend this model to incorporate the total upstream release as an additional exogenous predictor to complete the full characterization of (6b). The parameters $(\omega, \xi, \zeta, \gamma)$ are estimated using maximum likelihood [28]. We use the index j to refer to the upstream unit. This estimation captures how forecast uncertainty evolves in response to both intrinsic inflow variability and upstream operational decisions. The parameter ω represents the baseline variance level, ξ captures the impact of recent forecast errors, and ζ models volatility persistence over time. The coefficient γ quantifies the influence of upstream release and spill decisions on downstream forecast uncertainty, reflecting the physical propagation of flow variability through the cascade.

III. SOLUTION METHODOLOGY

Two approaches are proposed to solve the joint chance-constrained optimization problem in (1). The Bonferroni approximation decomposes the joint chance constraint into individual constraints using preset risk allocations, yielding a tractable but conservative reformulation based on marginal variance estimates. In contrast, the supporting hyperplane algorithm enforces the joint chance constraint directly by incorporating the full covariance structure of inflow uncertainty. This distinction is particularly important under decision-dependent uncertainty, where dynamic covariance coupling cannot be fully captured by marginal approximations.

A. Bonferroni Solution Algorithm

The Bonferroni approximation solves the joint chance constraint in (1g) by assuming spatial independence and decomposing the single chance constraint into a set of individual chance constraints whose combined violation probability is bounded through the union bound. The original joint chance constraint is

$$\mathbb{P}\left(\bigcap_{i=1}^n \underline{V}_i \leq v_{i,t} \leq \bar{V}_i\right) \geq 1 - \varepsilon, \quad (7)$$

After selecting the risk tolerance ε , each constraint i is allocated an equal violation budget ε_i such that

$$\varepsilon_i^{BON} = \frac{\varepsilon}{n}, \quad \sum_{i=1}^m \varepsilon_i = \varepsilon \quad (8)$$

By assuming a Gaussian form for the inflow forecasts, the individual chance constraints are reformulated into deterministic constraints by adding a safety margin that is the product of the standard normal quantile $z = \Phi^{-1}(1 - \varepsilon_i^{BON})$ and the standard deviation term. The deterministic volume bounds for unit i are given as

$$\underline{V}_i^{eff} = \underline{V}_i + z \hat{\sigma}_i \quad (9a)$$

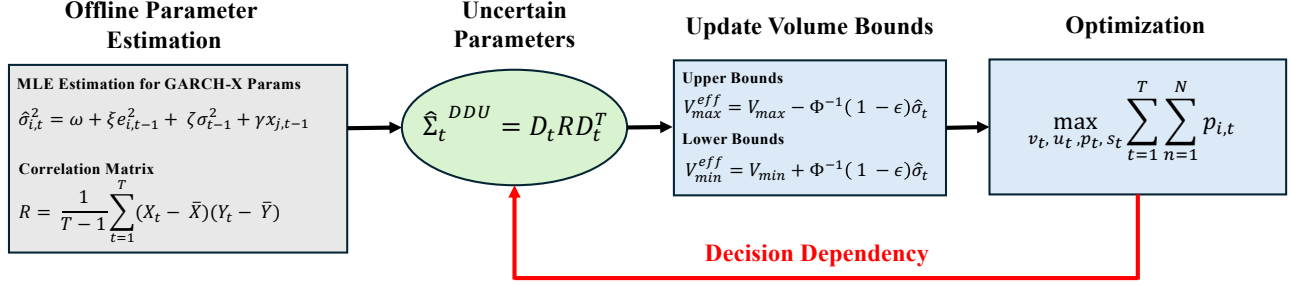


Fig. 3. Block diagram of online and state-dependent variance estimation

$$\bar{V}_i^{eff} = \bar{V}_i - z \hat{\sigma}_i \quad (9b)$$

Combining the substitution of the mean inflow forecast into (1b) and the safety bounds proposed in (9) completes the solution algorithm under the Bonferroni approximation. Note that the standard deviation estimated under both DIU and DDU is suitable for incorporating into the volume bounds. A key characteristic of the Bonferroni approximation is that it cannot adaptively relax or tighten its bounds, making it a simple, convex solution suitable for standard operating conditions and for moderate drought or flood events.

B. Supporting Hyperplane Solution Algorithm

The main limitation of the Bonferroni approximation is that it ignores the covariance structure of inflow uncertainty and relies on a static, exogenous risk split, which can be overly conservative or poorly calibrated in coupled systems. In cascaded hydropower networks, where inflows are both spatially correlated and decision-dependent, this simplification fails to capture how risk propagates across units.

To address this, we introduce the supporting hyperplane (SSH) algorithm, which enforces the joint chance constraint directly by leveraging the full multivariate distribution. By iteratively refining a polyhedral approximation of the feasible region using gradient information from the reliability function, SSH adaptively allocates risk while maintaining tractability and preserving the underlying dependence structure. We start by presenting the matrix representation of the linearized and convex optimization problem.

$$\min_{x_t \in \mathbb{R}^n, x \geq 0} c^T x_t \quad (10a)$$

$$\text{s.t. } A_t x_t \leq b_t \quad (10b)$$

$$v_t = v_{t-1} + \Delta_t (\hat{q}_t - u_t) \quad (10c)$$

$$\mathbb{P}[V_i \leq v_t \leq \bar{V}_i] \geq 1 - \epsilon \quad (10d)$$

where we define the per-timestep portion of each matrix as

$$A_t = \begin{pmatrix} 1 & -c\eta g \rho h_t^{ref} & 0 & 0 \\ 0 & 1 & 0 & 0 \\ 0 & -1 & 0 & 0 \\ 0 & 1 & 0 & 0 \\ 0 & -1 & 0 & 0 \\ 1 & 0 & 0 & 0 \end{pmatrix} \quad b_t = \begin{pmatrix} 0 \\ \bar{U} \\ -\underline{U} \\ \bar{R} + u_{t-1} \\ \underline{R} - u_{t-1} \\ \bar{P} \end{pmatrix}$$

$$x_t = \begin{pmatrix} p_t \\ u_t \\ s_t \\ v_t \end{pmatrix} \quad c_t = \begin{pmatrix} -1 \\ 0 \\ 1 \\ 0 \end{pmatrix}$$

The supporting hyperplane algorithm maintains spatial correlation between units and solves the joint chance constraint directly, requiring the cumulative distribution function (CDF) for the multivariate gaussian distribution that characterizes the inflow in the region. Evaluating the CDF over all the hydropower units allows us to identify which unit is the most at risk for violating volume boundaries. The general form of a CDF for $X \sim \mathcal{N}(\mu, \Sigma)$ at a points $a, b \in \mathbb{R}^n$ with $a_i \leq b_i$ is

$$F_X(a, b) = \mathbb{P}(a \leq X \leq b) = \int_{a_1}^{b_1} \dots \int_{a_n}^{b_n} f_X(t) dt \quad (11)$$

where $f_X(t)$ is the corresponding probability density function. We reformulate (7) to surround the random inflow variable \hat{q} by substituting the mass balance equation for v_t and recomputing the bounds.

$$\mathbb{P}[\underline{V}' \leq \hat{q}_t \leq \bar{V}'] \geq 1 - \epsilon \quad (12a)$$

$$\underline{V}' = \underline{V} - v_{t-1} + u_t \quad (12b)$$

$$\bar{V}' = \bar{V} - v_{t-1} + u_t \quad (12c)$$

Combining (11) and (12) derives an explicit formulation for evaluating the probability of volume bound violations given the current state.

$$F(\underline{V}', \bar{V}') = \frac{1}{(2\pi)^{n/2} |\hat{\Sigma}_t|^{1/2}} \int_{\underline{V}'_1}^{\bar{V}'_1} \dots \int_{\underline{V}'_n}^{\bar{V}'_n} e^{-\frac{1}{2}(x-\mu)^\top \hat{\Sigma}_t^{-1}(x-\mu)} dx \quad (13)$$

The CDF presented in (13) and its gradient can be numerically evaluated following the code in [29] and [30]. In practice, the finite difference method is sufficient for evaluating the gradient. The algorithm proposed in (1) is an extension of the methods from [19]. We adapt the algorithm to be solved sequentially and incorporate the real-time updates of the covariance matrix based in upstream release decisions.

Algorithm 1: Sequential Supporting Hyperplanes

Input : Solution x_t^{LP} to (10), a point x_t^s that is feasible for (10) and satisfies (12), and $\hat{\Sigma}_t$

Output: Solution x^* to (1)

for $t=1$ **to** T **do**

Initialization: $k=0, (x_t^0, A_t^0, b_t^0) \leftarrow (x_t^{LP}, A_t, b_t)$

while $\|x_t^{k+1} - x_t^k\|_\infty > tol$ **do**

Step 1: Interpolation

Find $\lambda^* \in (0,1)$

such that $x_t^{k*} = (1-\lambda^*)x_t^k + \lambda^*x_t^s$ and

$F[V'(x_t^{k*}), \bar{V}'(x_t^{k*})] \geq 1-\varepsilon$

Step 2: Add Cut

Add the hyperplane to the system

$\nabla F_k^T(x_t - x_t^{k*}) \leq 0$

$A_t^{k+1} \leftarrow A_t^k \cup \{\nabla F_k^T\}$ $b_t^{k+1} \leftarrow b_t^k \cup \{\nabla F_k^T x_t^{k*}\}$

Step 3: Solve the updated LP

Solve the updated linear program:

$x_t^{k+1} = \operatorname{argmin}\{c^T x_t \mid A_t^{k+1} x_t \leq b_t^{k+1}, x_t \geq 0\}$

if $\|x_t^{k+1} - x_t^k\|_\infty < tol$ **then**

break

end

$k \leftarrow k+1$

end

Store $x_t^* \leftarrow x_t^k$

Update $\hat{\Sigma}_{t+1}$

end

return x_t^*

Theorem 1. *The Sequential Supporting Hyperplane (SSH) algorithm either finds a global optimizer to the joint chance-constrained problem in a finite number of iterations or it generates a sequence $\{x_t^{k_i}\}_{i=1}^\infty$ converging to the global optimizer with tolerance ε_{LP} .*

The formal proof of convergence for the supporting hyperplane algorithm is given in Appendix B. The proof shows how the algorithm constructs a polyhedral approximation of the feasible region through hyperplane cuts that tighten the bounds on risky units while loosening the bounds on the safer units. This proof follows the structure of the convergence proof in [31]. We note that by construction, $\hat{\Sigma}_t^{DDU}$ is guaranteed to be positive definite and can be computed efficiently via the Cholesky decomposition.

A Slater point x_t^s is necessary for initializing the interpolation in Step 2. The equations used to determine x_t^s are given in (14), where we determine a feasible starting point by proposing a conservative release policy and calculating the next state. This ensures that x_t^s is feasible and will not violate volume bounds. The Slater point initialization algorithm is

$$u_t^s = \max\{\underline{U}, u_{t-1} - \underline{R}\} \quad (14a)$$

$$v_t^s = v_{t-1} + \Delta_t(\hat{q}_t - u_t^s) \quad (14b)$$

$$p_t^s = c\eta g\rho\phi_i(v_t^s)u_t^s \quad (14c)$$

where the release policy proposed in (14a) is the most conservative release policy available, either proposing full curtail-

ment or maintaining the minimum release level. The volume state and power generation are calculated in (14b) and (14c). We propose the SHS approach because it allows convergence across a broader set of scenarios, including more extreme drought events. When predefined reliability targets cannot be met, we instead identify the maximum achievable reliability that the system can guarantee under the given constraints.

C. Explicit Risk Attribution of SSH

One key advantage of SSH is its ability to endogenously allocate risk across units in a way that reflects the real-time system state and uncertainty structure. Unlike static approaches such as Bonferroni, which impose a uniform risk split regardless of operating conditions, SSH leverages sensitivity information from the joint reliability function to prioritize the most critical units. This raises a natural question: how does this adaptive allocation behave as the system approaches equilibrium? Theorem 2 addresses this by showing that, under steady-state conditions, the SSH allocation converges to the uniform Bonferroni rule, providing both theoretical grounding and interpretability for the method.

Theorem 2. *Under the state-state conditions, we see that the risk attribution weights in (22) converge to the Bonferroni bounds in (8).*

$$\varepsilon_i^{SSH} \rightarrow \frac{\varepsilon}{n} \quad (15a)$$

$$\varepsilon_i^{SSH} = \varepsilon\alpha_{i,t} \quad (15b)$$

The formal proof of this theorem is given in Appendix C. At a high level, Theorem 2 formalizes an intuitive equilibrium phenomenon in the risk allocation mechanism induced by the supporting hyperplane (SSH) algorithm. The key object is the *risk attribution signal* $\alpha_{i,t}$, which measures how sensitive overall system reliability is to marginal changes in each reservoir's state. When the system is away from steady state, for example, during transient drought dynamics, these sensitivities are heterogeneous because different units sit at different risk margins (some closer to violating bounds than others). The SSH algorithm exploits this heterogeneity by dynamically redistributing the total risk budget ε toward the most critical units via $\varepsilon_i^{SSH} = \varepsilon\alpha_{i,t}$. However, as the system converges and state updates become negligible ($\Delta x_t \rightarrow 0$), both the inflow distribution and the effective volume bounds become symmetric across units. In that regime, the gradients of the joint reliability function equalize, forcing $\alpha_{i,t} \rightarrow 1/n$, i.e., all units contribute equally to marginal system risk.

This yields a clear interpretation: the SSH framework is a *strict generalization* of Bonferroni risk allocation. In non-steady (operationally stressed or asymmetric) conditions, SSH behaves like an adaptive, state-aware allocator that prioritizes vulnerable units using the full covariance structure of uncertainty. In contrast, under steady-state conditions—where uncertainty, constraints, and system states are effectively homogeneous—the allocation collapses to the uniform rule $\varepsilon_i = \varepsilon/n$, exactly matching the Bonferroni approximation. This result shows that the additional complexity of SSH does

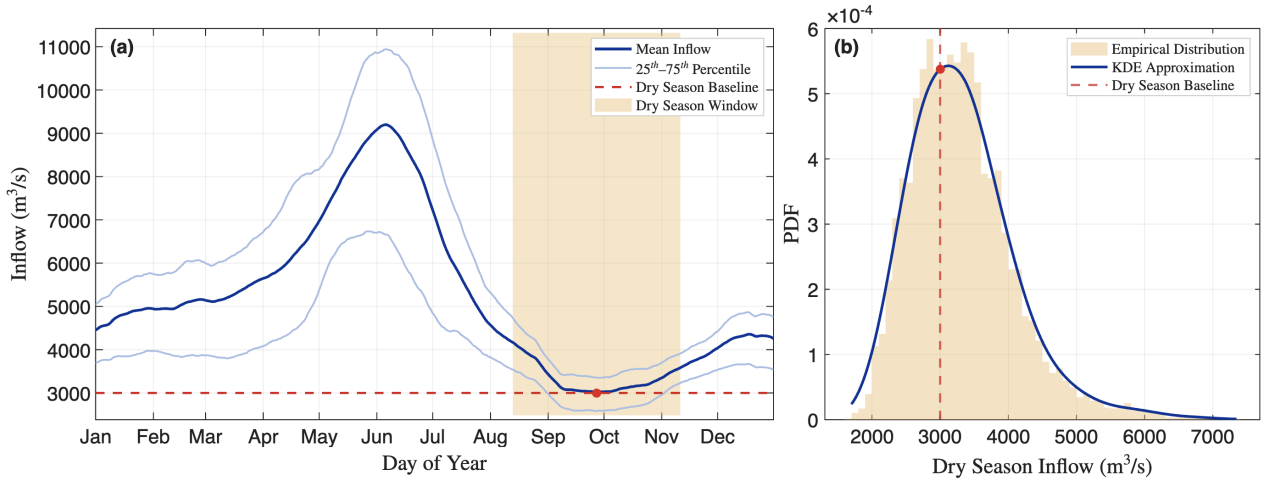


Fig. 4. Seasonal inflow behavior and dry-season baseline definition. (a) Seasonal hydrograph with interquartile variability and identified dry-season window. (b) Empirical distribution of dry-season inflows with kernel density estimate centered near the baseline flow

not distort classical intuition; rather, it recovers it as a limiting case. From an operational perspective, Bonferroni can be interpreted as the steady-state baseline, while SSH provides a principled mechanism for dynamically reallocating risk when system conditions justify asymmetric treatment across units.

IV. NUMERICAL STUDIES

A. Setup

We consider the real-time scheduling of a cascaded hydropower system consisting of three identical units in series. The nameplate capacity of each unit is 750 MW with a 90% generating efficiency. A nominal hydraulic head of 10m was used to represent typical operating conditions, with a ± 5 m operating band to capture realistic forebay variation. The minimum and maximum flow rates are 1,715 m³/s and 8,575 m³/s. The ramp rates are 1,715 m³/s/s and 2,572.5 m³/s/s for ramp-up and ramp-down capabilities respectively. The risk tolerance for violating volume bounds is set to $\varepsilon = 0.05$. The piece-wise linear approximation uses 40 segments for the power production function. The river system presented is a generalized approximation of the Columbia River. Fig. 4 shows how we used historical inflow data from the US Army Corps of Engineers¹ to construct the streamflow hydrograph and characterize the dry season inflow distribution. All case studies are conducted in MATLAB on a laptop with an Apple M3 4.1 GHz CPU and 16 GB of RAM. Gurobi 12.02 is used as the solver.

We set the travel time between hydro units to be $\tau = 1$, but note that this can be generalized. The mean inflow forecast is initially held constant between uncertainty frameworks for preliminary benchmarking. The set of parameters used in the mean inflow forecast are $(\alpha_0, \alpha_1, \beta_1, p, q) = (0.002, 0.95, 0, 1, 1)$. The normalized DIU standard deviation is estimated to be $\sigma^{DIU} = 0.002$. The normalized DDU coefficients for the GARCH-X model are $(\omega, \xi, \zeta, \gamma) = (0.0001, 0.008, 0, .003)$.

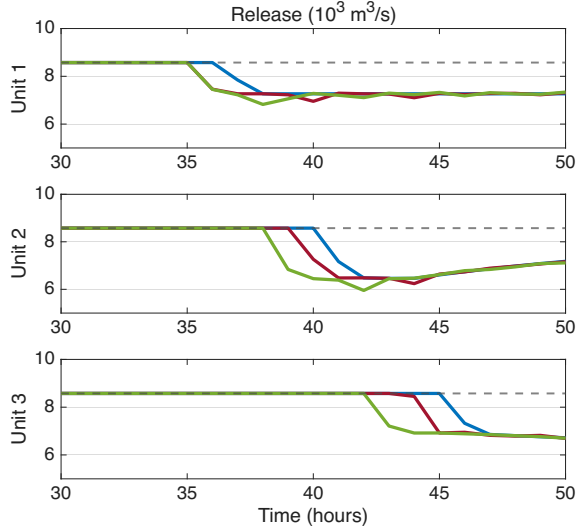
B. Policy Learning under Forecasted Droughts

During the dry season, hydropower operators face the challenge of maintaining both generation and minimum flow requirements while inflow is low and demand is high. Unexpected droughts can severely strain the system, requiring robust reliability measures to ensure the hydropower unit can maintain operations if inflow becomes unexpectedly constrained. We represent this by initializing all units to start with the initial volume condition of 10% capacity over 84 hourly periods, i.e. $\tau = \{1, \dots, 84\}$

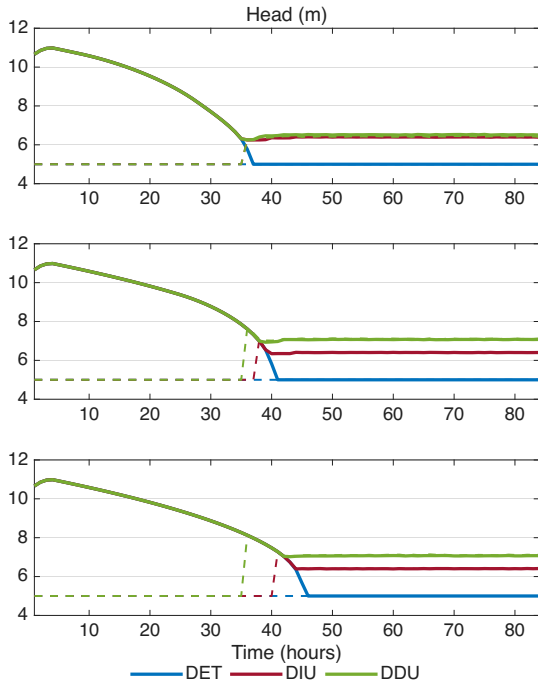
We derive drought scenarios by sampling from the joint distribution of base flow, drought duration, and intensity. Consider an initial estimation of the nominal streamflow to be $q_0 = 3,000$ m³/s, which is 15% below the maximum water release bound. The drought event is modeled as an exponential decay over 20 hours with a minimum amplitude scaled to be -15% of the nominal flow. The first 12 hours of the drought are the decay, and the final 8 hours are a linear restoration to the nominal flow. Each hydropower unit experiences one drought event, and the drought propagates between units over 16 hours. The baseline flow, amplitude, and duration used during Stage 1 policy training are the mean values from the distributions governing the drought characteristics. Let the deterministic uncertainty framework be abbreviated as DET and refer to the baseline scenarios in which inflow variance is set to zero for all units.

Fig. 5 compares the optimal policy trajectories for the cascaded hydropower units under drought conditions across uncertainty formulations under the supporting hyperplane solution method. Because the framework assumes the demand for electricity is larger than the generation capacity, all units are incentivized to ramp up water release to maximum flow rates until their storage is depleted. DDU alters the policy by curtailing releases earlier during the drought since it has an overall more conservative estimation of forecast uncertainty. Once the event subsides, all policies converge to the same steady-state release level with DDU resting at a higher hydraulic head due to its earlier conservation.

¹<https://www.nwd.usace.army.mil/crwm/water-control-data/project-data/>



(a)



(b)

Fig. 5. Optimal policy trajectories for water release and reservoir state under DET, DIU, and DDU uncertainty frameworks using the supporting hyperplane solution algorithm.

Table II summarizes the system performance under solution algorithms and uncertainty frameworks. It confirms the intuition that the more conservative safety buffers under DDU leads to a higher generation efficiency, a direct result of the nonlinear power production function increasing generation efficiency at higher forebay elevations. Therefore, DDU provides a mechanism for valuing storage under a single-period dispatch structure. We demonstrate the efficacy of the SSH algorithm by benchmarking it against the Bonferroni solution algorithm, noting that SSH achieves near optimal solution trajectories within numerical error.

TABLE II
BENCHMARKING ENERGY GENERATION AND EFFICIENCY

Alg.	Metric	DET	DIU	DDU
BON	Total [MWh]	122070	133480	137020
	Unit 1	39160	43420	43420
	Unit 2	40910	44740	46640
	Unit 3	42000	45310	46960
	Avg Sys [MW]	1450	1590	1630
	Avg Unit	480	530	540
	Eff.	17.63	19.35	19.93
SSH	Total [MWh]	122070	133390	137000
	Unit 1	39160	43360	43700
	Unit 2	40910	44720	46470
	Unit 3	42000	45310	46830
	Avg Sys [MW]	1450	1590	1630
	Avg Unit	480	530	540
	Eff.	17.63	19.34	19.92

C. Policy Testing under Stochastic Drought Scenarios

To test the release policies $u_{i,t}^{(m)*}$ learned during Stage 1 policy training under uncertainty framework m , we simulate the real-time reservoir volume trajectories under stochastic drought scenarios using Monte Carlo simulations. To quantify system performance, we define the integration violation index (IVI) as the total expected magnitude of the constraint violation across the simulation horizon. This metric quantifies the severity of the volume constraint violation over the entire system. It is defined as

$$IVI^{(m)} = \frac{1}{K} \sum_{k=1}^K \sum_{i=1}^N \sum_{t=1}^T \max(\underline{V}_i - v_{i,t}^{(k)}, 0) \quad (16)$$

Using Eq. 16, we define the violation rate of the learned policy as the average of its K trajectories violating the volume bounds.

$$\text{Violation Rate}(\%) = 100 \times \frac{1}{K} \sum_{k=1}^K \mathbf{1}(IVI_k > 0) \quad (17)$$

The testing procedure for each simulation $k=1, \dots, K$ is as follows:

- 1) Construct $q_t^{(k)}$ by sampling $q_0 \sim \mathcal{N}(\cdot)$, $\alpha \sim \beta(\cdot)$, and $D \sim \Gamma(\cdot)$ using the prior probability distributions
- 2) Simulate the real-time reservoir trajectory by sequentially updating volume state $v_{i,t}^{(k)} = v_{i,t-1}^{(k)} + q_{i,t}^{(k)} - u_{i,t}^{(m)*}$
- 3) Record the total energy production and IVI for each reservoir under the sampled inflow trajectory
- 4) Aggregate results and compute mean violation and mean energy production across simulations.

Fig. 6 examines the robustness of the release policy learned under the DDU framework and solved via SSH. It showcases how the learned policy trained under expected drought parameters ($\alpha = 15\%$, $D = 0.8$ days, $q_0 = 3000$ m³/s), performs across out of sample drought scenarios. We see that as amplitude and duration of the drought events increase, we are more likely to incur an operating violation. The trend remains for IVI, as drought duration and amplitude increase, so does the magnitude of the violation. Finally, we are able

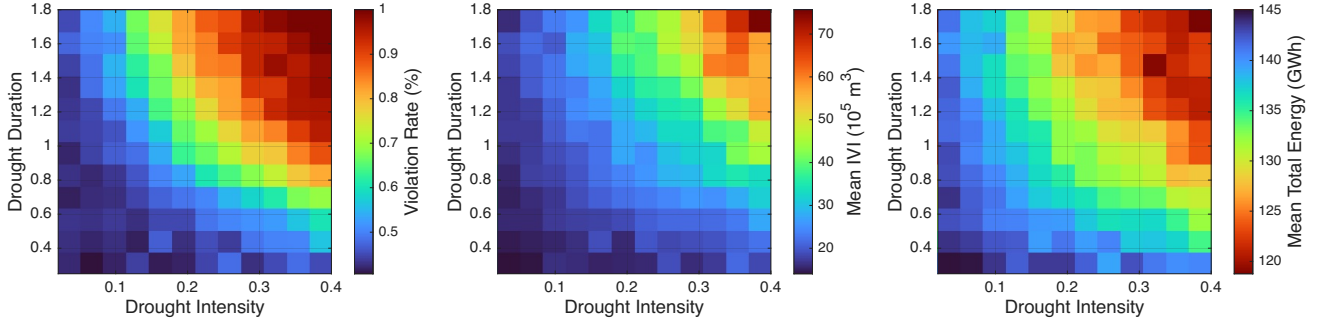


Fig. 6. Heatmaps of observed system performance under DDU and SSH from Monte Carlo simulations across drought amplitude (α) and duration (D). From left to right: violation rate (%), integrated violation index (m^3), and total system energy output (GWh).

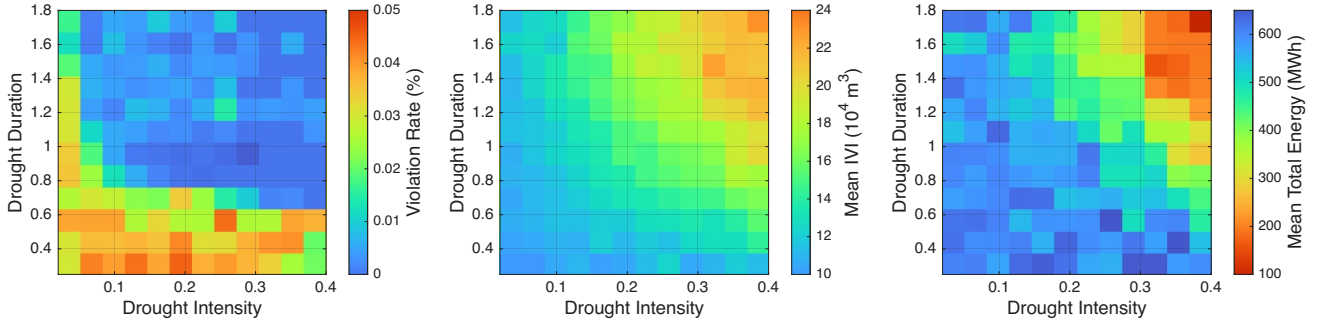


Fig. 7. Difference heatmaps showing the magnitude of change between DIU and DDU policies from Monte Carlo simulations across drought amplitude (α) and duration (D). From left to right: violation rate (%), integrated violation index (m^3), and total system energy output (GWh).

to observe increase energy generation across the system when the drought is milder.

Fig. 7 compares how the policy learned under DIU compares to the policy learned under DDU by using a difference heatmap. The left most plot compares the difference in violation rate (DIU-DDU). We see that for more intense droughts in the upper right, the two policies confirm that a constraint violation is unavoidable. However, for the milder droughts in the lower left, DDU reduces the violation rate across scenarios. We can confirm this observation by examining the difference in IVI (DIU - DDU). Across all scenarios, policies learned under DDU consistently reduce the magnitude of violation. Finally, we compare system energy generation (DDU - DIU) and show how policies learned under DDU are able to extract more energy from the same inflow profile. Therefore, DDU both increases system efficiency while enhancing system reliability under stochastic drought scenarios.

The advantage of the supporting hyperplane algorithm over the Bonferroni approximation is that when the system is faced with extreme drought scenarios, it can still guarantee convergence even when the allotted risk tolerance isn't able to be met. This property is a unique feature of the SSH algorithm and arises from its ability from evaluating the joint probability distribution directly while making the hyperplane cuts, as seen in (22). We can leverage this latent state to compare the performance of SSH and BON on extreme drought events using the following procedure. We first initialize the test by

- 1) Sweep over the set of drought parameters (α, q_0) to determine the inflow trajectories where BON and SSH converge.

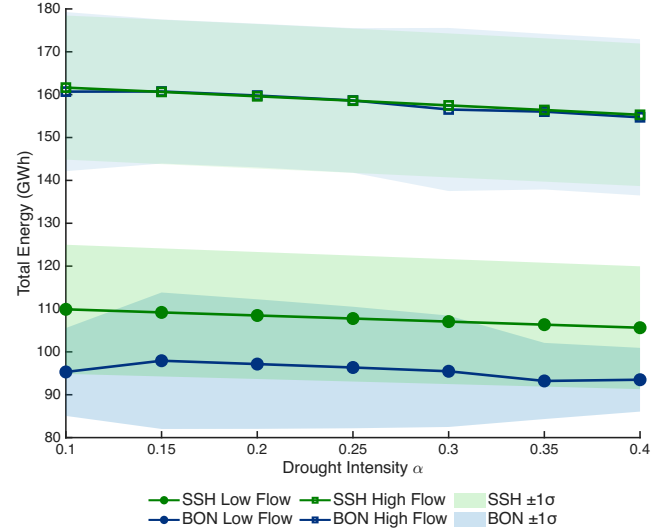


Fig. 8. Mean total energy under drought scenarios for SSH (green, proposed) and BON (blue, benchmark). Circle and square markers indicate low- and high-flow regimes

- 2) Store the release policies for each cell where the program converges for each solution algorithm.
- 3) Record the convergence criteria in $\phi_{\text{BON}}(a, d)$ and $\phi_{\text{SSH}}(a, d)$

The convergence behavior of the two solution methods differs significantly across drought conditions. For the Bonferroni (BON) approximation, convergence is binary—either a feasible solution is obtained or the problem fails under the

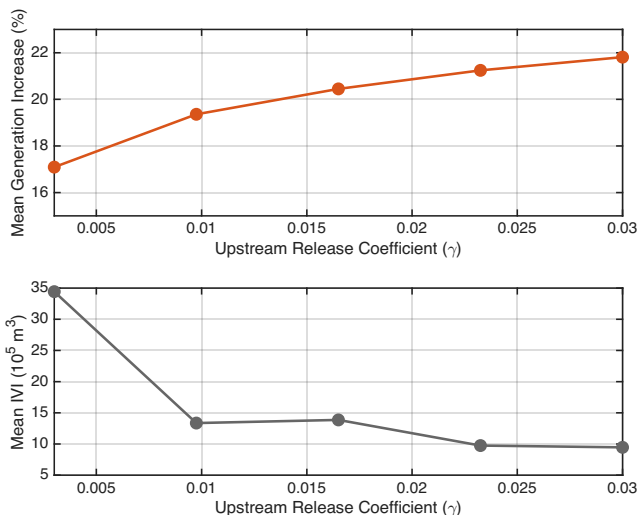


Fig. 9. Average generation increase (top) and system-wide constraint violation (bottom) across upstream release coefficients, averaged over forecast error coefficient.

specified parameters. In contrast, the SSH formulation always returns a solution and provides the corresponding minimum reliability guarantee. Using the policies recorded for each parameter cell, we proceed with the following evaluation:

- 4) For each drought parameter $\alpha^{(a)}$ and $q_0^{(d)}$, retrieve the corresponding inflow realization $q_{a,d}$.
- 5) If $\phi_{\text{BON}}(a, d)$ has not converged, replace $X_{\text{BON}}(a, d)$ with the state trajectory from the nearest converged cell (a^*, d^*) , determined by minimizing Euclidean distance over all feasible entries.
- 6) Simulate both policies forward to obtain reservoir volumes V , releases u , and total energy generation for each policy.

Fig. 8 visualizes the results of this testing procedure through difference maps $\Delta E = E_{\text{SSH}} - E_{\text{BON}}$. Each point corresponds to the optimal solution of the joint chance-constrained model under a given drought scenario. The SSH formulation converges over a broader set of severe conditions and yields a corresponding reliability guarantee, whereas BON frequently fails to converge in extreme regimes, resulting in fewer feasible solutions. Consequently, SSH is able to extract more energy from the system across a wider range of drought scenarios.

D. Sensitivity Analysis

A sensitivity analysis is performed on the GARCH model parameters (ξ, γ) in order to understand how model tuning impacts system performance. The parameters used Stage 1 policy training were used as the baseline, and we added an amplification coefficient to sweep the parameters upwards. Note that ξ represents the coefficient for weight forecast errors. In real world parameter tuning, it was determined that this coefficient was 0.8. Fig. 9 demonstrates how in our simulations, this coefficient is not very impactful. This was motivated us to scale the coefficient down to its 0.008 value used in policy learning such that the estimated standard deviations were not inflated. We see that γ plays a large role

in modifying system performance. Simply put, larger gamma values indicate a more conservative estimate of forecast error for the inflow model. A conservative estimation of real-time inflow forecast error is rewarded in the hydropower setting, and leads to more energy extraction. This is because the system is more sensitive to in-network decisions, and encourages the system to end at a larger steady-state value leading to more high hydraulic head and higher energy efficiency.

V. CONCLUSION

The strategic conservation under DDU leads to higher storage levels and therefore higher hydraulic head later in the horizon, enabling the system to produce more power from the same release volume. In effect, the DDU policy's short-term water savings translate directly into greater long-term value, making it the most revenue-efficient strategy when its uncertainty assumptions align with the true inflow dynamics. Future work will investigate how the derived risk allocation signals from the supporting hyperplanes algorithm can be used to restore reservoir operations to a safe level under extreme droughts and floods. Furthermore, adding in a mechanism to quantify the value of storage will solidify the methods here in the medium-term planning framework. It's important to balance immediate benefit versus future benefit, especially when straddling multiple time horizons.

REFERENCES

- [1] M. Ho, U. Lall, X. Sun, and E. R. Cook, "Multiscale temporal variability and regional patterns in 555 years of conterminous us streamflow," *Water Resources Research*, vol. 53, no. 4, pp. 3047–3066, 2017.
- [2] Z. He, S. Bolognani, F. Dörfler, and M. Muehlebach, "Decision-dependent stochastic optimization: The role of distribution dynamics," *arXiv [math.OA]*, Mar. 2025.
- [3] B. Tong, Q. Zhai, and X. Guan, "An MILP based formulation for short-term hydro generation scheduling with analysis of the linearization effects on solution feasibility," *IEEE Trans. Power Syst.*, vol. 28, no. 4, pp. 3588–3599, Nov. 2013.
- [4] T. M. Souza, "An accurate representation of water delay times for cascaded reservoirs in hydro scheduling problems," in *2012 IEEE Power and Energy Society General Meeting*. IEEE, Jul. 2012, pp. 1–7.
- [5] X. Ge, L. Zhang, J. Shu, and N. fan Xu, "Short-term hydropower optimal scheduling considering the optimization of water time delay," *Electric Power Systems Research*, vol. 110, pp. 188–197, 2014. [Online]. Available: <https://api.semanticscholar.org/CorpusID:109644386>
- [6] Z. Wang, F. Wu, Y. Li, J. Li, Y. Liu, and W. Liu, "Day-ahead dispatch approach for cascaded hydropower-photovoltaic complementary system based on two-stage robust optimization," *Energy*, vol. 265, p. 126145, 2023.
- [7] C. Ju, T. Ding, W. Jia, C. Mu, H. Zhang, and Y. Sun, "Two-stage robust unit commitment with the cascade hydropower stations retrofitted with pump stations," *Applied Energy*, vol. 334, p. 120675, 2023.
- [8] A. Helseth and B. Mo, "Hydropower aggregation by spatial decomposition—an sddp approach," *IEEE Transactions on Sustainable Energy*, vol. 14, no. 1, pp. 381–392, 2022.
- [9] X. Wu, C. Cheng, J. R. Lund, W. Niu, and S. Miao, "Stochastic dynamic programming for hydropower reservoir operations with multiple local optima," *Journal of Hydrology*, vol. 564, pp. 712–722, 2018.
- [10] J. E. Nash, "The form of the instantaneous unit hydrograph," *IAHS Publication*, vol. 45, pp. 114–121, 1957.
- [11] J. C. I. Dooge, "Linear theory of hydrologic systems," *Technical Bulletin, U.S. Department of Agriculture*, vol. 1468, 1973.
- [12] K. Beven, *Rainfall-Runoff Modelling: The Primer*, 2nd ed. Wiley, 2012.
- [13] A. Sharma, D. G. Tarboton, and U. Lall, "Streamflow simulation: A nonparametric approach," *Water resources research*, vol. 33, no. 2, pp. 291–308, 1997.

- [14] F. Pianco, A. Moreira, B. Fanzeres, R. Jiang, C. Zhao, and M. Heleno, "Decision-dependent uncertainty-aware distribution system planning under wildfire risk," *IEEE Transactions on Power Systems*, 2025.
- [15] B. Hu, C. Pan, C. Shao, K. Xie, T. Niu, C. Li, and L. Peng, "Decision-dependent uncertainty modeling in power system operational reliability evaluations," *IEEE Transactions on Power Systems*, vol. 36, no. 6, pp. 5708–5721, 2021.
- [16] N. Qi, N. Zheng, and B. Xu, "Chance-constrained energy storage pricing for social welfare maximization," *arXiv [eess.SY]*, Jul. 2024.
- [17] S. Giannelos, I. Konstantelos, and G. Strbac, "Option value of demand-side response schemes under decision-dependent uncertainty," *IEEE Transactions on Power Systems*, vol. 33, no. 5, pp. 5103–5113, 2018.
- [18] C. Ordoudis, V. A. Nguyen, D. Kuhn, and P. Pinson, "Energy and reserve dispatch with distributionally robust joint chance constraints," *Oper. Res. Lett.*, vol. 49, no. 3, pp. 291–299, May 2021.
- [19] W. van Ackooij, R. Henrion, A. Moller, and R. Zorgati, "Joint chance constrained programming for hydro reservoir management," *Optim. Eng.*, vol. 15, no. 2, pp. 509–531, Oct. 2013.
- [20] J.-C. Alais, P. Carpentier, and M. De Lara, "Multi-usage hydropower single dam management: chance-constrained optimization and stochastic viability," *Energy Syst.*, vol. 8, no. 1, pp. 7–30, Feb. 2017.
- [21] E. Cohn, N. Qi, U. Lall, and B. Xu, "A lagrangian-informed long-term dispatch policy for coupled hydropower and photovoltaic systems," in *2025 IEEE Power & Energy Society General Meeting (PESGM)*. IEEE, Jul. 2025, pp. 1–5.
- [22] H. Zhang, K. Liao, J. Yang, Z. Yin, and Z. He, "Long-term and short-term coordinated scheduling for wind-PV-hydro-storage hybrid energy system based on deep reinforcement learning," *IEEE Trans. Sustain. Energy*, vol. PP, no. 99, pp. 1–13, 2025.
- [23] W. Yuan, S. Zhang, C. Su, Y. Wu, D. Yan, and Z. Wu, "Optimal scheduling of cascade hydropower plants in a portfolio electricity market considering the dynamic water delay," *Energy (Oxf.)*, vol. 252, no. 124025, p. 124025, Aug. 2022.
- [24] J. Kong, H. I. Skjeltved, and O. B. Fosso, "An overview on formulations and optimization methods for the unit-based short-term hydro scheduling problem," *Electric Power Syst. Res.*, vol. 178, no. 106027, p. 106027, Jan. 2020.
- [25] B. A. Faber and J. R. Stedinger, "Reservoir optimization using sampling SDP with ensemble streamflow prediction (ESP) forecasts," *J. Hydrol. (Amst.)*, vol. 249, no. 1-4, pp. 113–133, Aug. 2001.
- [26] J. D. Hamilton, *Time series analysis*. Princeton, NJ: Princeton University Press, 1994.
- [27] T. Bollerslev, "Modelling the coherence in short-run nominal exchange rates: A multivariate generalized arch model," *Rev. Econ. Stat.*, vol. 72, no. 3, p. 498, Aug. 1990.
- [28] A. Meister and J.-P. Kreib, "Statistical inference for nonparametric GARCH models," *Stoch. Process. Their Appl.*, vol. 126, no. 10, pp. 3009–3040, Oct. 2016.
- [29] A. Genz, "Numerical computation of multivariate normal probabilities," *J. Comput. Graph. Stat.*, vol. 1, no. 2, pp. 141–149, Jun. 1992.
- [30] W. Van Ackooij, R. Henrion, A. Moller, and R. Zorgati, "On probabilistic constraints induced by rectangular sets and multivariate normal distributions," *Math. Methods Oper. Res. (Heidelb.)*, vol. 71, no. 3, pp. 535–549, Jun. 2010.
- [31] J. Kronqvist, A. Lundell, and T. Westerlund, "The extended supporting hyperplane algorithm for convex mixed-integer nonlinear programming," *J. Glob. Optim.*, vol. 64, no. 2, pp. 249–272, Feb. 2016.
- [32] A. Prekopa and T. Szantai, "Flood control reservoir system design using stochastic programming," in *Mathematical Programming in Use*. Berlin, Heidelberg: Springer Berlin Heidelberg, 1978, pp. 138–151.

APPENDIX

A. Linear Approximation

A piece-wise linear approximation is applied to the nonlinear power production function to complete the convex parameterization of the original problem.

- 1) Calculate the N sub-intervals $I_i = [h_{i-1}, h_i]$ for $i = 1, 2, \dots, N$ where $h_0 = h_{\min}$ and $h_N = h_{\max}$
- 2) Determine the optimal reference elevation $h_i^{\text{ref}} = \text{argmin}_{h \in I_i} \mathbb{E}[\|g(h, u) - g(h_i^{\text{ref}}, u)\|^2]$
- 3) Create the reference vector $H^{\text{ref}} = [h_1^{\text{ref}}, h_2^{\text{ref}}, \dots, h_N^{\text{ref}}]$

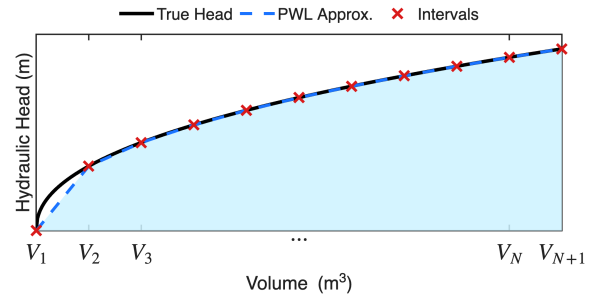


Fig. 10. Illustration of the piece-wise linear approximation of hydraulic head function over a normalized volume range with 10 sub-intervals.

This algorithm is well-suited to apply a convex parameterization over the bilinear term by calculating the hydraulic head reference from the previous volume term. During real-time scheduling, the algorithm is implemented as follows

- 1) Calculate the forebay elevation $h_t = \phi(v_{t-1})$
- 2) Find sub-interval index $i^* = \text{arg max}_i \{h_t \in I_i\}$ and retrieve the reference elevation $h^{\text{ref}} = h_{i^*}^{\text{ref}}$
- 3) Approximate the power production function $p_t \approx c\eta g p h^{\text{ref}} u_t$

We visualize the piece-wise linear approximation of the hydraulic head function in Fig. 10.

The volume has been normalized to enable comparison between units with different storage capacities while preserving the nonlinear relationship between storage and head. We note that this function defines why generation efficiency is reduced at low storage levels.

B. Proof of Theorem 1

Proof: First note that the function $\varphi_t(x)$ is logarithmically concave under Gaussian distributions and its feasible set $\Omega_t = \{x_t : \varphi_t(x_t) \geq p\}$ is convex. This is an established property from Prekopa in [32]. Using this property, we can establish the monotonic refinement relationship. Namely

$$\Omega_t \subseteq \mathcal{P}_t^K \subseteq \dots \subseteq \mathcal{P}_t^1 \subseteq \mathcal{P}_t^0 \quad (18)$$

where $\mathcal{P}_t^k = \{x_t \geq 0 : A_t^k x_t \leq b_t^k\}$ is the feasible region generated by solving the LP at iteration k and time t . We establish this result by noting the result x_t^k obtained from solving the LP implies that $\varphi_t(x_t^k) < p$ and $x_t^k \notin \Omega_t$. Since $\varphi_t(\cdot)$ is continuous, the intermediate value theorem guarantees the existence of $\lambda^* \in (0, 1]$ that finds x_t^{k*} such that $\varphi_t(x_t^{k*}) = p$ with tolerance ε_R . Because $\varphi_t(\cdot)$ is concave at x_t^{k*} , the supporting hyperplane generated at iteration k and time t establishes the following

$$p \leq \varphi_t(x_t) \leq \varphi_t(x_t^{k*}) + \nabla \varphi_t(x_t^{k*})^T (x_t - x_t^{k*}) \quad (19a)$$

$$p \leq \varphi_t(x_t) \leq p + \nabla \varphi_t(x_t^{k*})^T (x_t - x_t^{k*}) \quad (19b)$$

$$0 \leq \nabla \varphi_t(x_t^{k*})^T (x_t - x_t^{k*}) \quad (19c)$$

$$-\nabla \varphi_t(x_t^{k*})^T x_t \leq -\nabla \varphi_t(x_t^{k*})^T x_t^{k*} \quad (19d)$$

Note that the hyperplane constraint separates x_t^k from the estimated feasible region and establishes monotonic refinement. If the SSH algorithm terminates after K iterations,

x_t^{K+1} is optimal the solution to the LP defined by \mathcal{P}_t^K . By the upper boundary of stopping criteria, we establish that

$$\frac{c^T(x_t^{K*} - x_t^{K+1})}{c^T x_t^{K+1}} = \varepsilon_{LP} \quad (20a)$$

$$x_t^{K*} = (1 + \varepsilon_{LP})x_t^{K+1} \quad (20b)$$

Therefore, x_t^{K*} gives the optimal value to the objective function of the joint chance-constrained program with tolerance ε_{LP} in the feasible region of \mathcal{P}_t^K . From Eq. (18), we know that \mathcal{P}_t^K includes the feasible set Ω_t . Since x_t^{K*} satisfies the joint chance constraint $\varphi(x_t^{K*}) \geq p$, it is also in the feasible region Ω_t . Because x_t^{K*} minimizes the objective function within \mathcal{P}_t^K and $x_t^{K*} \in \Omega_t$, x_t^{K*} is also an optimal solution at time t . We concatenate all of the optimal decisions x_t^* for $t = [1, \dots, T]$ to form the optimal decision vector x^* over the entire horizon.

The sequence will generate at least one convergent subsequence $\{x_t^{k_i}\}_{i=1}^\infty$ if it does not converge in a finite number of iterations. We remark that sets $\{\mathcal{P}_t^0, \mathcal{P}_t^1, \dots\}$ are compact because they are generated from a series of intersecting half-spaces and the original feasible region of the original problem, which is a closed and bounded subset of Euclidean space. Therefore, $\{x_t^{k_i}\}_{i=1}^\infty$ is a bounded sequence of real numbers and it has a convergent subsequence by the Bolzano-Weierstrass theorem.

Next, we show that the limit point of a convergence subsequence $\{x_t^{k_i}\}_{i=1}^\infty$ is a global minimum. Because each set \mathcal{P}_t^k overestimates Ω_t , $c^T x_t^{k_i}$ gives a lower bound on the optimal value of the objective function. From the monotonic refinement relation and its corollary on separating hyperplanes, we know that $\{c^T x_t^{k_i}\}_{i=1}^\infty$ is non-decreasing. We can also conclude that $\lim_{i \rightarrow \infty} c^T x_t^{k_i} = c^T \tilde{x}_t$, where $\tilde{x}_t \in \Omega_t$ is the limit point of the sequence. Therefore, the SSH algorithm will generate a sequence converging to the global optimum.

C. Proof of Theorem 2

Let the system reliability with respect to volume bounds be defined in (13) as $F(\underline{V}'_t, \bar{V}'_t)$. Note that $F(\cdot)$ is log-concave, monotonically non-decreasing, right-continuous, and differentiable when $\Sigma_t \succ 0$. We define gradient of the system reliability with respect to the volume state as

$$\frac{\partial F_t}{\partial v_{i,t-1}} = -\frac{\partial F_t}{\partial \underline{V}'_{i,t}} - \frac{\partial F_t}{\partial \bar{V}'_{i,t}} \quad (21)$$

which is calculated from applying the chain rule directly

$$\frac{\partial F_t}{\partial v_{i,t-1}} = \sum_{k=1}^n \left(\frac{\partial F_t}{\partial \underline{V}'_{k,t}} \frac{\partial \underline{V}'_{k,t}}{\partial v_{i,t-1}} + \frac{\partial F_t}{\partial \bar{V}'_{k,t}} \frac{\partial \bar{V}'_{k,t}}{\partial v_{i,t-1}} \right).$$

From the definitions of \underline{V}'_t and \bar{V}'_t ,

$$\frac{\partial \underline{V}'_{k,t}}{\partial v_{i,t-1}} = \frac{\partial \bar{V}'_{k,t}}{\partial v_{i,t-1}} = -\mathbf{1}\{k=i\},$$

which yields

$$\frac{\partial F_t}{\partial v_{i,t-1}} = -\frac{\partial F_t}{\partial \underline{V}'_{i,t}} - \frac{\partial F_t}{\partial \bar{V}'_{i,t}}.$$

The expression relates how the contribution of the volume state to system reliability for each hydropower unit is proportional the effective inflow bounds, motivating the introduction of the "risk attribution signal", which we define

$$\alpha_{i,t} = \frac{\left| \frac{\partial F_t}{\partial v_{i,t-1}} \right|}{\sum_{j=1}^n \left| \frac{\partial F_t}{\partial v_{j,t-1}} \right|} \quad (22)$$

Where $\alpha_{i,t}$ is a measure of how strongly each unit contributes to the overall probability system remains in the safe operating region. If the inflow distribution and state-to-bound mappings are symmetric across units, then

$$\left| \frac{\partial F_t}{\partial v_{1,t-1}} \right| = \dots = \left| \frac{\partial F_t}{\partial v_{n,t-1}} \right|,$$

and

$$\alpha_{i,t} = \frac{1}{n}, \quad \forall i.$$

This is equivalent to showing that under the steady-state conditions $\Delta x_t \rightarrow 0$, the risk attribution weights become equal across all units, such that

$$\alpha_{1,t} = \dots = \alpha_{n,t}$$

Because the denominators for $\alpha_{i,t}$ are identical for $\forall i$, this is equivalent to showing

$$\left| \frac{\partial F_t}{\partial v_{1,t-1}} \right| = \dots = \left| \frac{\partial F_t}{\partial v_{n,t-1}} \right|$$

Which can be equivalently rewritten using (21) as

$$\frac{\partial F_t}{\partial \underline{V}'_{1,t}} + \frac{\partial F_t}{\partial \bar{V}'_{1,t}} = \dots = \frac{\partial F_t}{\partial \underline{V}'_{n,t}} + \frac{\partial F_t}{\partial \bar{V}'_{n,t}}$$

Next, we show the upper bound gradients are equal across all units during steady state. To do this, we state the define the gradient of (13) with respect to boundary conditions as

$$\frac{\partial}{\partial b_i} F_\xi(a,b) = f_{\xi_i}(b_i) F_{\xi_i^c}(a, \tilde{b}) \quad (23a)$$

$$\frac{\partial}{\partial a_i} F_\xi(a,b) = -f_{\xi_i}(a_i) F_{\xi_i^c}(\tilde{a}, b) \quad (23b)$$

following [30], where f_{ξ_i} is the corresponding probability density function, and $F_{\xi_i^c}(\tilde{a}, \tilde{b})$ denotes the two-side cumulative distribution function with the contribution from component a_i removed. It is defined symmetrically for b_i as well. We have already shown that the risk attribution weights are defined by the linear combination of volume bounded gradients. Using (12), we note that \underline{V}' and \bar{V}' are functions of the control policies, which we can write explicitly as $\underline{V}'(x_t)$ and $\bar{V}'(x_t)$. Plugging in our definitions to the general form of (23), we show that when $\Delta x_t \rightarrow 0$

$$\frac{\partial}{\partial \bar{V}'_1(x_t)} F_\xi(\underline{V}', \bar{V}') = \dots = \frac{\partial}{\partial \bar{V}'_n(x_t)} F_\xi(\underline{V}', \bar{V}')$$